14th International Symposium on Turbulence and Shear Flow Phenomena (TSFP14)
Heidelberg, Germany, July 28–31, 2026

RESPONSE OF TURBULENT BAND FORMATION TO TEMPORALLY DECREASING REYNOLDS NUMBER IN PLANE CHANNEL FLOW

Ryoko Ono[1], **Kazuki Kohyama**[2], **Yuki Matsukawa**[1,3], **Takahiro Tsukahara**[1]
[1]Department of Mechanical and Aerospace Engineering, Tokyo University of Science
2641 Yamazaki, Noda-shi, Chiba 278-8510, Japan
[2]Space Environment and Energy Laboratories, NTT, Inc.
3-9-11 Midori-cho, Musashino-shi, Tokyo 180-8585, Japan
[3]Department of Mechanical Engineering, Meiji University
1-1-1 Higashi-Mita, Tama-ku, Kawasaki-shi, Kanagawa 214-8571, Japan
7525512@ed.tus.ac.jp, kazuki.kohyama@ntt.com, matsukawa@meiji.ac.jp, tsuka@rs.tus.ac.jp

ABSTRACT

Subcritical transitions in wall-bounded shear flows lead to the coexistence of laminar and turbulent regions, manifesting as spatio-temporally intermittent structures such as oblique turbulent bands in channel flows. This study investigates the formation and sustenance of such bands using direct numerical simulations of plane Poiseuille flow under deceleration and subsequent transient conditions. The time scales are determined by varying the rate of decrease in a nominal friction Reynolds number, and by adjusting the computational domain size according to the scales of the target structures. After deceleration, seeds of turbulent bands are found to remain sparsely distributed and evolve transiently into banded structures. The spatial distribution of these seeds is distinct from that of fully developed bands in equilibrium states. The results demonstrate that insufficient computational domain size relative to the seed spacing leads to probabilistic band formation.

INTRODUCTION

Wall-bounded shear flows exhibit spatio-temporally intermittent turbulent structures in their subcritical transition below the linear stability threshold (Manneville, 2016). The intermittent structures, known as turbulent puffs or turbulent bands, appear near the global-stability critical Reynolds number Re_G, which marks the lower boundary of turbulent maintenance (Tuckerman *et al.*, 2020). For the pipe flow, Avila *et al.* (2011) measured the time scales of turbulent puff splitting and decay, and determined Re_G, at which these two time scales are comparable. This finding may support Pomeau (1986), that proposed a link between the directed percolation (DP) phenomenon in non-equilibrium statistical physics and the subcritical turbulent transition. For a comprehensive discussion, the reader is referred to Hof (2023).

As for the plane Poiseuille flow, laminar–turbulent banded patterns have been discussed from multiple complementary perspectives. Localized bands act as fundamental building blocks of transition (Tao *et al.*, 2018), which can be triggered when perturbations exceed a minimal energy threshold (Parente *et al.*, 2022). These structures organize into oblique stripe patterns that correspond to exact coherent solutions of the Navier–Stokes equations (Paranjape *et al.*, 2020) and can be interpreted within a bifurcation framework (Shimizu & Manneville, 2019). From a different viewpoint, the uniform turbulent flow itself becomes linearly unstable, leading to spatial modulation and pattern formation (Kashyap *et al.*, 2022), whose dynamics follow nonlinear bifurcation scenarios and scaling laws (Kashyap *et al.*, 2025). Experimental observations have confirmed the physical realization of such patterns (Hashimoto *et al.*, 2009; Paranjape, 2019; Yimprasert *et al.*, 2021), while statistical approaches including numerical observations described the transition as DP processes (Sano & Tamai, 2016; Shimizu & Manneville, 2019; Takeda & Tsukahara, 2019). In this context, localized turbulent bands have been shown to exhibit memoryless dynamics when their size is fixed; however, their lifetime depends strongly on band length, implying that in realistic flows with evolving structures, effective memory effects cannot be neglected (Xu & Song, 2022). Consistently, recent work by Vasudevan *et al.* (2025) has shown that band dynamics cannot be fully captured by Markovian (memoryless) statistical descriptions, suggesting that the transition is unlikely to follow DP and that a band growth mechanism fundamentally alters the nature of the transition to turbulence compared to pipe flow.

An open question remains as to the extent to which the aforementioned statistical results are influenced by the finite size of the experimental channel, as in Sano & Tamai (2016). Their channel length from the inlet to the observation area ensures a dimensionless travel time of $O(10^1–10^2)$, which is much shorter than the estimated time scale of $O(10^7–10^8)$ required to balance the puff split and decay in the pipe flow experiment of Avila *et al.* (2011). This discrepancy has prompted questions about the validity of the channel flow experiment. In order to assess the experimental observations reported by Sano & Tamai (2016), it is important to clarify the time scale over which localized turbulence attains a statistically steady state. To this end, we numerically investigate the persistence of turbulence by gradually decreasing the nominal friction Reynolds number, Re_τ, from a fully turbulent state. The target structures for time-scale analysis include not only large-scale turbulent bands, but also near-wall streaks governed by viscous-scale dynamics. To capture both different scale structures, we systematically vary the computational domain size to elucidate domain-size effects on the deceleration response. As listed in Table 1, four computational domain sizes were employed: S, smaller than a turbulent band but larger than streaks; M, comparable to a single turbulent band; L, sufficiently large to capture multiple bands; and XL, substantially larger than the band scale. We performed several DNSs to investigate the response of localized turbulence patterns to a decrease in Re_τ from a fully developed turbulent state at various time scales and in different computational domain sizes.

Table 1: Computational conditions and number of trials for the DNS of plane Poiseuille flow: L_i^*, the domain size in i direction, non-dimensionalized by δ; N_i, the number of grid points; and ΔT^*, the deceleration time.

Case	$L_x^* \times L_y^* \times L_z^*$ ($N_x \times N_y \times N_z$)	ΔT^*	Number of trials
SA		0.8	10
SB	$12.8 \times 2 \times 12.8$	7.8	10
SC	$(256 \times 96 \times 256)$	78	10
SD		780	20
MA		0.8	10
MB	$51.2 \times 2 \times 51.2$	7.8	10
MC	$(1024 \times 96 \times 1024)$	78	10
MD		780	10
LA		0.8	10
LB	$102.4 \times 2 \times 102.4$	7.8	10
LC	$(512 \times 64 \times 512)$	78	10
LD		780	10
XLB	$4096 \times 2 \times 512$ $(32768 \times 64 \times 8192)$	8.0	1

The transient behavior following a reduction in the Reynolds number was also investigated in detail. In particular, after a moderate deceleration, the intermittent structures respond with a delay, and transient dynamics persist even after the Reynolds number is held constant. During this transient phase, we focus on the spatial distribution of naturally occurring localized turbulent structures, which are considered to represent "seeds" of turbulent bands.

NUMERICAL METHOD

The plane Poiseuille flow, the target of this study, is a flow driven by a uniform pressure gradient (in x) between two parallel plates. The two walls are separated by a gap width of 2δ in the y-direction, while z denotes the spanwise direction. The governing equations are the incompressible continuity equations and Navier–Stokes equations.

We performed DNSs using our finite-difference code to accurately reproduce the turbulence and its reverse transition phenomena. The code is based on the same formulation as that used in our previous works (Tsukahara *et al.*, 2005; Kohyama *et al.*, 2022). We imposed periodic boundary conditions in the x- and z-directions and no-slip conditions at both walls. Table 1 summarizes the computational settings, including the domain sizes and the number of grid points. The cases are labeled, in order of increasing domain size, as Case-S*, Case-M*, Case-L*, and Case-XL*. The asterisk is replaced by A–D, which denote the cases in order of decreasing deceleration rate, as described later. Although the grid resolution differs, this does not affect the main conclusions of the present study.

The control parameter is the friction Reynolds number, $Re_\tau \equiv u_\tau \delta / \nu$, where ν is the kinematic viscosity and u_τ is the friction velocity, which is determined by the imposed pressure gradient. We investigated the flow response in two consecutive phases: a deceleration phase, during which the nominal Re_τ decreases linearly from $Re_{\tau,\text{start}}$ to $Re_{\tau,\text{end}}$ over a duration ΔT; and a transient phase, which continues from the end of the deceleration until the flow field reaches equilibrium at the fixed $Re_{\tau,\text{end}}$. The initial flow to be decelerated is taken from an arbitrary snapshot of a fully turbulent state at $Re_{\tau,\text{start}} = 150$. While the actual Re_τ, defined by the instantaneous wall shear stress, may fluctuate, the nominal Re_τ is monotonically reduced to $Re_{\tau,\text{end}}$. We chose $Re_{\tau,\text{end}} = 54$, which remains above Re_G. This allows the emergence of localized turbulence in sufficiently large computational domains (Kohyama *et al.*, 2022).

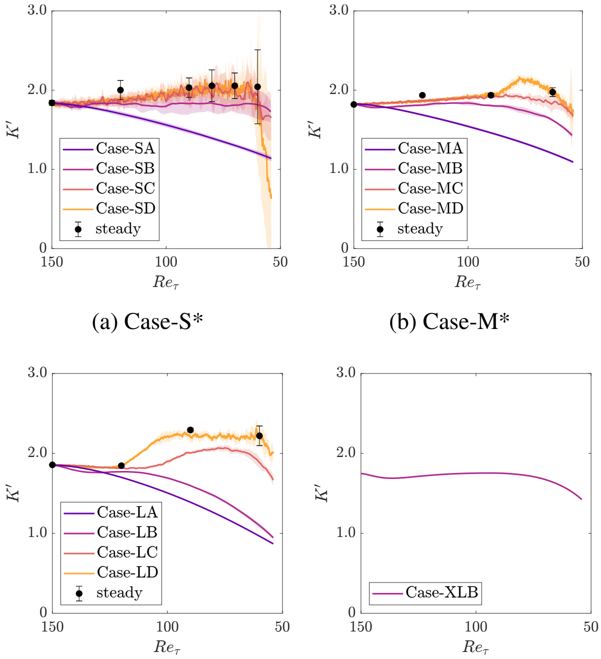

(a) Case-S* (b) Case-M*

(c) Case-L* (d) Case-XL*

Figure 1: Temporal evolution of turbulent kinetic energy in response to changes in the nominal friction Reynolds number during the deceleration phase. Solid lines indicate ensemble-averaged values, and shaded areas represent the standard deviation. Black symbols denote the steady-state values obtained from well-developed flow fields at each fixed Re_τ.

The duration ΔT, over which the nominal Re_τ decreases at a constant rate from $Re_{\tau,\text{start}}$ to $Re_{\tau,\text{end}}$, is another important parameter. As shown in Table 1, ΔT was varied over four different orders of magnitude, which are non-dimensionalized by δ/u_τ. They are referred to as Case-*A, Case-*B, Case-*C, and Case-*D, in order of decreasing deceleration rate. For example, Case-SA represents the smallest computational domain combined with the steepest deceleration rate, whereas Case-XLB corresponds to the largest domain with a moderate deceleration. The deceleration was applied to multiple initial turbulent fields at $Re_{\tau,\text{start}} = 150$ to obtain ensemble-averaged results for each case.

RESULT AND DISCUSSION

Figure 1 shows the temporal evolution of the averaged turbulent kinetic energy during the deceleration phase. Here, we employ the spatial average of the turbulent kinetic energy over the entire domain as an indicator of the flow state:

$$K' = \frac{1}{L_x L_y L_z} \int_0^{L_z} \int_0^{L_y} \int_0^{L_x} \frac{1}{2} \left(u'u' + v'v' + w'w' \right) \mathrm{d}x\mathrm{d}y\mathrm{d}z \quad (1)$$

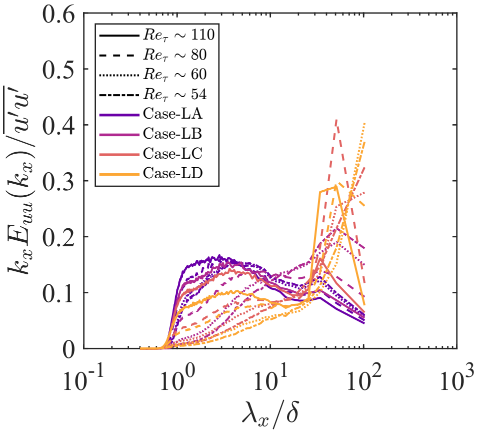

(a)

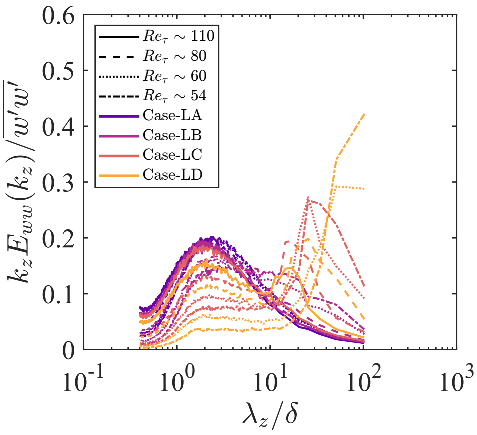

(b)

Figure 2: Pre-multiplied energy spectra during the deceleration phase in Case-L: (a) $k_x E_{uu}/\overline{u'u'}$ and (b) $k_z E_{ww}/\overline{w'w'}$. Each line style represents a different Reynolds number, while the line color indicates the deceleration condition (shorter deceleration time in purple and longer in yellow). The spectra are plotted at representative instants for each Reynolds number during the deceleration phase.

where (u, v, w) are the velocity components in (x, y, z), and $(\ )'$ denotes the fluctuation from the spatial mean. When the flow field is laminar, K' should be 0. For each case, the mean and variance are computed based on at least 10 independent trials. All panels in Fig. 1 reveal that the abrupt deceleration in Case-*A leads to a monotonic decrease in K'. Although K' does not vanish at the end of the deceleration phase, it eventually decays to zero during the transient phase (not shown). This behavior is independent of the computational domain size. Interestingly, in larger domains, K' even increases above its initial value at $Re_{\tau,\mathrm{start}}$, followed by the appearance of a plateau. These values are consistent with the DNS results at equilibrium (symbols in the figure), indicating that the effect of temporal deceleration is insignificant in Case-*D. This implies that $\Delta T^* = 780$ should be longer than the time scale of the turbulent band.

Figure 2 shows the distributions of the pre-multiplied energy spectra during the deceleration phase for Case-L*, in which the dependence on ΔT^* is clearly manifested. The spectra are extracted at instants when the nominal Re_τ reaches prescribed values. The pre-multiplied spectra allow evaluation of the dominant wavelength and its containing energy. Here, particular attention is paid to long-wavelength components of $O(10^1)$ or larger. The results show that, in Case-LA,

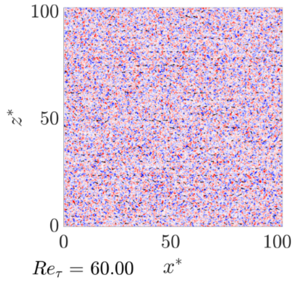

(a) Case-LA ($\Delta T^* = 0.8$)

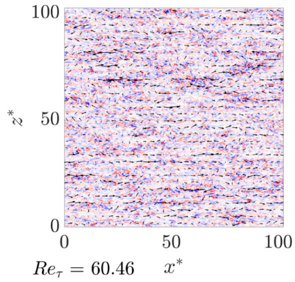

(b) Case-LB ($\Delta T^* = 7.8$)

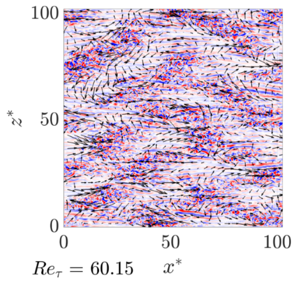

(c) Case-LC ($\Delta T^* = 78$)

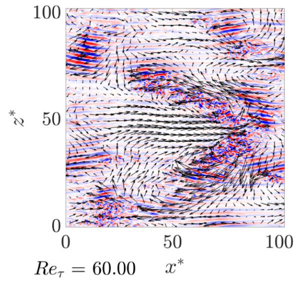

(d) Case-LD ($\Delta T^* = 780$)

Figure 3: Instantaneous flow fields in the channel-central x–z plane at the nominal $Re_\tau \approx 60$. Contours show $v' > |1|$, and vectors of (u', w') are averaged over local $3.2\delta \times 3.2\delta$.

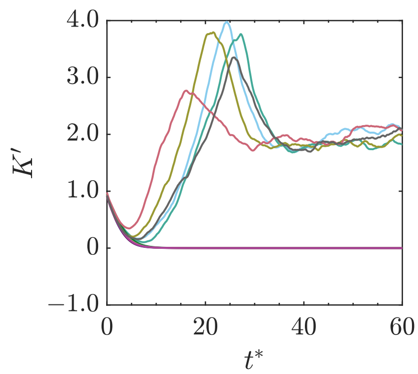

Figure 4: Time evolution of K' from the end of the Re_τ-reduction phase ($t = 0$) for ten trials in Case-LB; five sustain turbulence, and five decay to a fully laminar state.

no distinct peak is observed in the long-wavelength range. In contrast, in Case-LD, a signature of a long-wavelength peak emerges from $Re_\tau \approx 110$. The wavelengths λ_x and λ_z larger than 10δ, observed in the u' and w' components, do not correspond to near-wall turbulent structures such as streaks or quasi-streamwise vortices, but instead indicate the presence of large-scale secondary flows (LSFs) aligned with turbulent bands or stripes. Corresponding instantaneous flow fields and LSFs at a nominal $Re_\tau \approx 60$ for each ΔT^* are shown in Fig. 3. For $\Delta T^* \geq 78$, the onsets of spatial intermittency and LSFs are observed. In particular, as shown in panel (c), well-developed turbulent bands can be identified. Such band formation is also observed in Case-LD (Fig. 3(d)) and -MD (not shown), where the bands emerge and persist as an equilibrium state. In contrast, a small ΔT^* does not allow the formation of turbulent bands and LSFs, as shown in Fig. 3(a, b). Similarly, in Case-S*, the flow relaminarizes without forming turbulent bands, although the corresponding visualizations are omitted here.

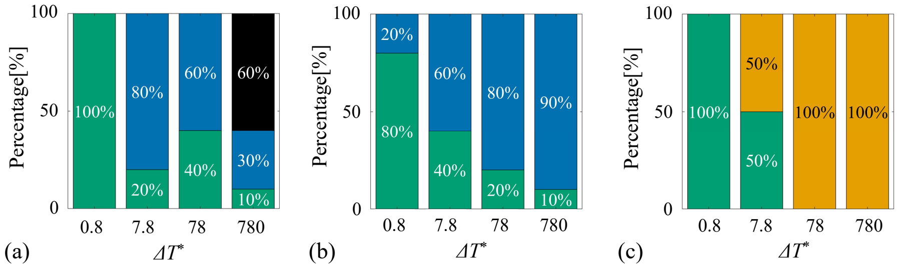

Figure 5: Percentage of each flow-response type observed during the transient phase: (a) Case-S*, (b) Case-M*, and (c) Case-L*. Orange indicates Type-1 (sustained intermittent turbulence), blue Type-2 (temporarily sustained intermittent turbulence), green Type-3 (monotonic laminarization during the transient phase), and black Type-4 (laminarization completed during the deceleration phase).

Hereafter, we focus on the transient phase at constant Re_τ after the deceleration phase, as shown in Fig. 4. In Case-LB, the post-transient behavior can be classified into two distinct outcomes, which are determined probabilistically by the initial condition (i.e., the timing of deceleration in turbulent states). From ten realizations with randomly selected deceleration timings, five trials exhibit a monotonic decay to the laminar state ($K' = 0$), whereas the remaining five show a transient growth after reaching a minimum in K', eventually attaining an equilibrium state. The equilibrium state is identical among all five realizations. Extending this analysis to other cases, the flow responses are classified into four types, taking into account the transient phase: Type-1, stably sustained intermittent turbulence with banded patterns; Type-2, temporarily sustained intermittent turbulence; Type-3, monotonic laminarization during the transient phase; and Type-4, laminarization during the deceleration phase. Figure 5 shows the occurrence rates of four types for each case. In Case-LB corresponding to $\Delta T^* = 7.8$ in panel (c), Type-1 and -3 occur with equal probability (50% each), as shown above. Notably, Type-1 occurs with a probability of 100% for $\Delta T^* \geq 78$, as shown in Fig. 5(c). When the computational domain is sufficiently larger than the turbulent band, as in Case-L*, the stochasticity of relaminarization is suppressed, allowing the critical deceleration rate to be determined more clearly. Based on these results, the time scale required for the maintenance of turbulent bands is estimated to be on the order of $O(10^1)$, as revealed by the DNS results in the large computational domain (Case-L*), indicating a characteristic time scale for sustaining turbulent bands. This time scale is shorter than the travel time $O(10^1–10^2)$ in Sano & Tamai (2016), supporting the view that their observation window was long enough for band formation. In panel (b), the occurrence rates of Type-2 and -3 tend to increase and decrease, respectively, with increasing ΔT^*, suggesting that the flow behavior in each category depends on the deceleration rate. These probabilistic behaviors observed also in Case-LB are inferred to outcome from the interplay between the computational domain size and the spatial scale of the "seed of turbulent spots," which will be shown in the following. Accordingly, we further focus on the spatial distribution of such seeds captured in the larger computational domain of Case-XL, and examine how their characteristics, together with the emergence of LSFs, influence band growth and the maintenance of turbulence.

Figure 6 shows a representative realization of Case-LB in which the turbulent stripe is ultimately sustained, corresponding to the cyan curve in Fig. 4. At the instant immediately after the end of the deceleration phase, shown in Fig. 6(a), neither clear intermittency nor LSFs are observed. At the instant of minimum K', shown in (b), a single seed of a turbulent spot can be identified near the center of the domain. Although weak disturbances are still present elsewhere, only one seed

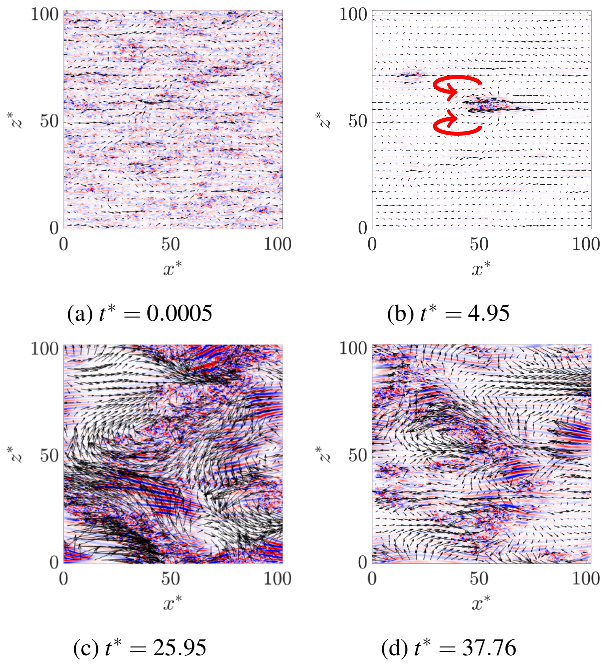

Figure 6: Instantaneous flow fields in the channel-central x–z plane at four instants during the transient phase for one representative realization of Case-LB. Contours show $v' > |1|$, and vectors of (u', w') are averaged over local $3.2\delta \times 3.2\delta$.

develops into a turbulent spot and subsequently into a band. The black vectors in the figure represent the in-plane velocity field obtained by applying a low-pass filter. Focusing on the vicinity of the seed, a characteristic flow structure, as indicated by the red arrows, can be observed, which is in good agreement with observations of minimal seeds reported by Parente *et al.* (2022), suggesting that the observed structures correspond to dynamically relevant minimal seeds. Figure 6(c) corresponds to the instant when K' reaches a transient maximum, where the LSFs appear stronger than in the subsequent state (d) (a quantitative assessment of its intensity is provided later). Whether turbulence is sustained in Case-LB is determined by the flow state at the minimum of K' in (b). Since the seeds are sparsely distributed—so sparse that only a single seed is captured within a $102.4\delta \times 102.4\delta$ domain—cases in which no seed is captured are likely to relaminarize.

To clarify the sparse spatial distribution of seeds, the result for Case-XLB is shown in Fig. 7. Although the exact times differ, four instants equivalent to those visualized in Fig. 6 are extracted, and the entire computational domain is displayed. The characteristic features observed at each instant are con-

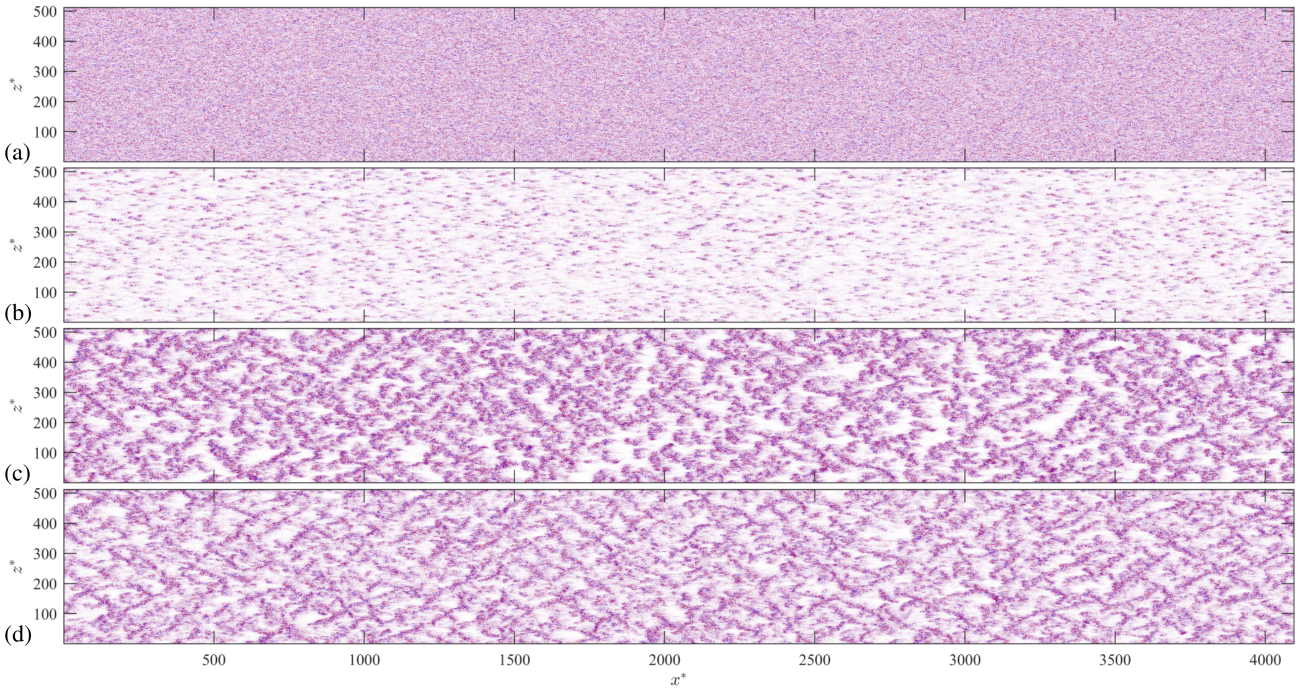

Figure 7: Instantaneous flow fields in the channel-central x–z plane, visualized by the wall-normal velocity fluctuation $v' > |1|$, during the transient phase for Case-XLB, at (a) $t^* = 0.0005$ (just after the end of deceleration phase), (b) $t^* = 5.25$ (closest to the minimum K'), (c) $t^* = 14.6$ (maximum K'), and (d) $t^* = 20.5$ (state close to the statistically steady condition), respectively.

sistent with those identified in Case-LB. Of particular interest is the spatial distribution of seeds in Fig. 7(b). Although numerous seeds are distributed throughout the domain, their mutual spacing can be estimated to be approximately 100δ (note that both coordinate axes are normalized by δ). Therefore, in small-domain DNS where no seed is captured within the computational domain during the deceleration phase, the flow ultimately relaminarizes. The probability of such relaminarization decreases as the domain size increases, and when the domain size is sufficiently larger than 100δ, seeds are captured with near certainty, leading to sustained turbulence in the form of band and stripe patterns.

To provide a more detailed view of the flow field, including LSFs, Fig. 8 presents magnified snapshots of a $200\delta \times 200\delta$ region. The reference frame is translated downstream to follow the propagation of intermittent structures such as spots and bands, whose convection velocity is approximately equal to the bulk velocity (Fukudome & Iida, 2012). Immediately after the end of the deceleration phase, shown in panel (a), neither intermittency nor large-scale patterns are observed. As the disturbance subsequently decays, seeds become sparsely distributed at the instant of minimum K'. Compared with Fig. 6(b), the seeds appear more densely distributed. This observation is consistent with Figs. 1(c, d), where K' remains larger in Case-XLB during the later stage of deceleration. Although Case-LB is considered to capture the intrinsic structures of turbulence during the deceleration phase, the dependence on the computational domain size at this scale still warrants further discussion. From Fig. 8(b), signatures of LSFs can be identified, with a characteristic scale on the order of 100δ. At this stage, the LSFs are predominantly aligned with the streamwise direction (highlighted by red circles), and oblique LSFs are not yet prominent. In panels (c) and (d), oblique LSFs and band structures become apparent. Although the spatial arrangement of the bands is not strictly regular, the spatial scale of the LSFs remains approximately constant, as

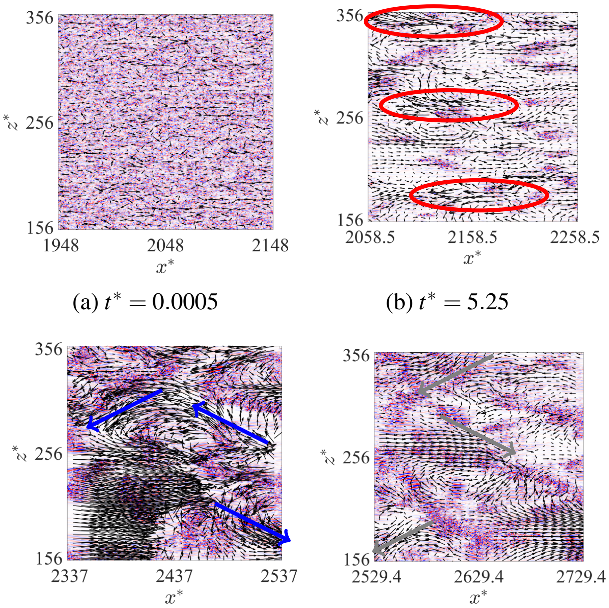

(a) $t^* = 0.0005$ (b) $t^* = 5.25$

(c) $t^* = 14.6$ (d) $t^* = 20.5$

Figure 8: Same as in Fig. 7, but showing magnified views with vectors of (u', w') averaged over local $8\delta \times 8\delta$. The reference frame translates in time to follow the propagation of turbulent bands. Circles and arrows highlight LSFs.

indicated by the blue and gray arrows. From the sequence of (b)–(d), it is evident that both LSFs and patterns are not stationary within the observation period, suggesting that the modulation of these patterns occurs on a time scale of $O(10^0$–$10^1)$.

To quantify the large-scale pattern formation observed above, as well as the sparse distribution of seeds (and the associated LSFs), premultiplied energy spectra are employed

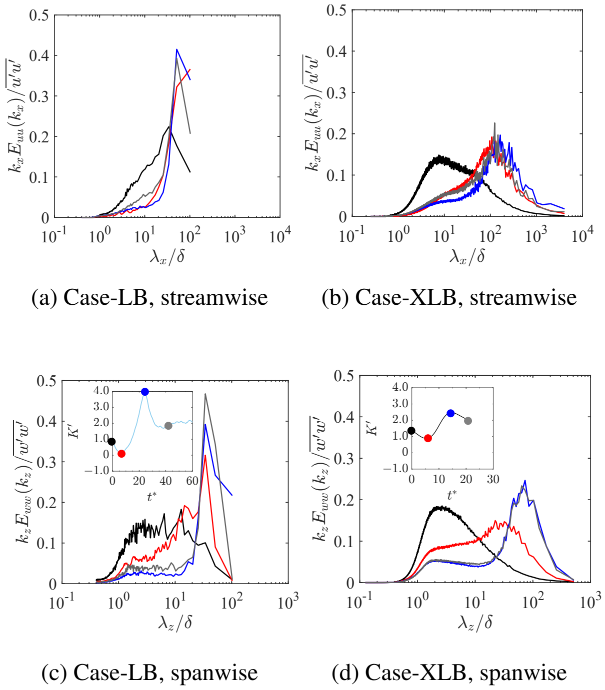

(a) Case-LB, streamwise (b) Case-XLB, streamwise

(c) Case-LB, spanwise (d) Case-XLB, spanwise

Figure 9: Pre-multiplied energy spectra at representative instants during the transition phase: (a,b) $k_x E_{uu}/\overline{u'u'}$ and (c,d) $k_z E_{ww}/\overline{w'w'}$. In panel (c,d), a small inset shows the temporal evolution of the turbulent kinetic energy. The circular markers indicate the instants corresponding to each colored spectra.

again. Figure 9 shows the spectra in both the streamwise and spanwise directions, for the corresponding wavelengths (k_x, k_z) and velocity components (u', w'). A comparison with Case-LB reveals that, in the long-wavelength range, Case-XLB captures the full spectral bandwidth containing significant energy, and that the peak wavelengths differ between the two cases. In the seed-dominated regime (indicated by the red line), the peak wavelength in the streamwise direction is located at $\lambda_x \approx 100\delta$, and it slightly increases during the formation of stripe patterns. The peak λ_z changes in time and differs significantly between the seed-dominated and stripe regimes. These temporal variations are not captured in Case-LB.

CONCLUSION

We performed DNS of plane channel flow in the subcritical Reynolds number regime where laminar–turbulent banded patterns emerge, and investigated the flow response during and after deceleration. The characteristic time scale for turbulent band formation is $t^* \sim O(10)$. This finding lends support to the reliability of the observation conditions of Sano & Tamai (2016), in terms of the band-formation time scale. After deceleration, the seeds of turbulent bands remain dispersed with a spacing of approximately 100δ, from which bands transiently develop. This spacing differs from that of developed bands or stripe in equilibrium states. Small domain relative to the seed spacing leads to probabilistic turbulent band formation.

ACKNOWLEDGMENT

The present DNSs were performed using supercomputers at the Cyberscience Center of Tohoku Univ. and the D3 Center of The Univ. of Osaka. This study was partially supported by JSPS KAKENHI Grant Number 24KJ2023, 26K07361.

REFERENCES

Avila, K., Moxey, D., de Lozar, A., Avila, M., Barkley, D. & Hof, B. 2011 The onset of turbulence in pipe flow. *Science* **333** (6039), 192–196.

Fukudome, K. & Iida, O. 2012 Large-scale flow structure in turbulent poiseuille flows at low-Reynolds numbers. *Journal of Fluid Science and Technology* **7** (1), 181–195.

Hashimoto, S., Hasobe, A., Tsukahara, T., Kawaguchi, Y. & Kawamura, H. 2009 An experimental study on turbulent-stripe structure in transitional channel flow. In *Turbulence Heat and Mass Transfer 6: Proceedings of the Sixth International Symposium on Turbulence Heat and Mass Transfer*. Begel House Inc.

Hof, B. 2023 Directed percolation and the transition to turbulence. *Nature Reviews Physics* **5** (1), 62–72.

Kashyap, P.V., Duguet, Y. & Dauchot, O. 2022 Linear instability of turbulent channel flow. *Physical Review Letters* **129**, 244501.

Kashyap, P.V., Marín, J.F., Duguet, Y. & Dauchot, O. 2025 Laminar-turbulent patterns in shear flows: Evasion of tipping, saddle-loop bifurcation, and log scaling of the turbulent fraction. *Physical Review Letters* **134**, 154001.

Kohyama, K., Sano, M. & Tsukahara, T. 2022 Sidewall effect on turbulent band in subcritical transition of high-aspect-ratio duct flow. *Physics of Fluids* **34** (8), 084112.

Manneville, P. 2016 Transition to turbulence in wall-bounded flows: where do we stand? *Mechanical Engineering Reviews* **3** (2), 15–00684.

Paranjape, C.S., Duguet, Y. & Hof, B. 2020 Oblique stripe solutions of channel flow. *Journal of Fluid Mechanics* **897**, A7.

Paranjape, Chaitanya S 2019 Onset of turbulence in plane Poiseuille flow. PhD thesis, IST Austria.

Parente, E., Robinet, J.-Ch., De Palma, P. & Cherubini, S. 2022 Minimal energy thresholds for sustained turbulent bands in channel flow. *Journal of Fluid Mechanics* **942**, A18.

Pomeau, Y. 1986 Front motion, metastability and subcritical bifurcations in hydrodynamics. *Physica D* **23** (1), 3–11.

Sano, M. & Tamai, K. 2016 A universal transition to turbulence in channel flow. *Nature Physics* **12** (3), 249–253.

Shimizu, M. & Manneville, P. 2019 Bifurcations to turbulence in transitional channel flow. *Phys. Rev. Fluids* **4**, 113903.

Takeda, K. & Tsukahara, T. 2019 Subcritical transition of plane Poiseuille flow as (2+1)d and (1+1)d DP universality classes. In *Abstract of the Eighth Symposium on Bifurcations and Instabilities in Fluid Dynamics*. ID: 175.

Tao, J.J., Eckhardt, B. & Xiong, X.M. 2018 Extended localized structures and the onset of turbulence in channel flow. *Physical Review Fluids* **3** (1), 011902.

Tsukahara, T, Seki, Y, Kawamura, H & Tochio, D 2005 DNS of turbulent channel flow at very low Reynolds numbers. In *Proceedings of the Fourth International Symposium on Turbulence and Shear Flow Phenomena*, pp. 935–940.

Tuckerman, L. S., Chantry, M. & Barkley, D. 2020 Patterns in wall-bounded shear flows. *Annual Review of Fluid Mechanics* **52** (1), 343–367.

Vasudevan, M., Paranjape, C.S., Sitte, M.P., Yalniz, G. & Hof, B. 2025 Aging and memory of transitional turbulence. *Nature Communications* **16**.

Xu, D. & Song, B. 2022 Size-dependent transient nature of localized turbulence in transitional channel flow. *Journal of Fluid Mechanics* **950**, R3.

Yimprasert, S., Kvick, M., Alfredsson, P.H. & Matsubara, M. 2021 Flow visualization and skin friction determination in transitional channel flow. *Experiments in Fluids* **62** (2), 31.